Computational Fluid Dynamics Simulations of the Transonic Dynamics Tunnel Airstream Oscillator System

Robert E. Bartels[1] and Pawel Chwalowski[2]
NASA Langley Research Center, Hampton, VA, 23681

This paper presents computational fluid dynamics simulations of the flow in the NASA Langley Research Center Transonic Dynamics Tunnel (TDT) with the airstream oscillator system (AOS) in operation. Test section flow angle can be modulated using sinusoidally oscillating vanes which are located in pairs within the contraction section of the tunnel circuit. A compilation of previously published experimental data for validation has been reviewed that contains hot-wire anemometer and fast-response probe data acquired in an empty test section with the vanes oscillating in-phase and out-of-phase. These experimental data have not previously been compared with computational results. The present results provide an opportunity for validation of the simulations of the sinusoidal AOS flow field in the TDT test section. Computed tunnel centerline, lateral and cross-section contour data of flow angle and vorticity show that resolving the vane tip vortex is critical to accurately predicting the test section center flow angle. The computed results show, as do the experimental data, what appears to be a resonance at higher frequencies. It is currently not known what is the cause of that resonance. Further refinement of the mesh is expected to improve the comparisons with experimental data.

I.   Introduction

This paper presents a Computational Fluid Dynamics (CFD) model of the flow in the NASA Langley Research Center Transonic Dynamics Tunnel (TDT) with the Airstream Oscillator System (AOS) in operation. The TDT is a continuous-flow, closed-circuit wind tunnel with a 16- by 16-foot slotted test section with cropped corners. The tunnel was originally built as the 19-ft Pressure Tunnel in 1938, but it was converted to the current transonic tunnel in the 1950s, with capabilities to use either air or heavy gas (R-12, later R-134a) as the test medium. The TDT was also fitted with an AOS, which can be used to create a gust field in the test section. To date, no computational analyses of the TDT involving the AOS in operation have been performed.

Previous CFD simulations of the empty TDT without the AOS have validated the model with experimental wall pressure and boundary layer rake measurements [1, 2]. Simulations of an atmospheric boundary layer (ABL) impacting a launch vehicle model using Irwin spires [3] have compared very well with experimental data. In another example, computational simulations of a full-span fighter configuration installed in the TDT have shown that wall effects and blockage within the TDT test section do not affect the flutter onset [2]. In some cases, computational methods can be considered mature enough to complement or supplant wind-tunnel testing. However, in the transonic regime, modeling the wind-tunnel flow environment is more difficult and requires further refinement of simulation parameters. This is expected to be the case when simulating the TDT AOS in operation in the transonic regime.

The purpose of this paper is to validate a computational model of the TDT AOS with the intent that it can some day be used to compute and perhaps predict the gust response of an aeroelastic model in the wind tunnel. For the

---

present paper, the CFD model will be validated by comparing computed vertical flow velocity angles in an empty tunnel to experimental flow angles recorded in the TDT literature [4–6]. In addition to a validation of this model with experimental data, it may also be possible to supplement the experimental data with additional computed data. The experimental data are rather sparse and at only a few Mach numbers, but it is recognized that computational results may be able to expand the AOS data set. Another motivation for this work is a complex aeroelastic test program involving the Integrated Adaptive Wing Technology Maturation (IAWTM) semispan model of the high-aspect-ratio CRM with 10 trailing edge control surfaces [7, 8]. This model is currently being fabricated and will be delivered to the NASA Langley TDT for testing in 2021. Among tests to be conducted using the IAWTM model, gust load alleviation (GLA) will be demonstrated at transonic conditions using the AOS.

II. TDT AOS Overview

The TDT AOS is comprised of short oscillating vanes that protrude from the tunnel walls to produce a sinusoidal disturbance in the tunnel flow. Figure 1, with Figure 2, shows the location of the AOS in the TDT. The view in Figure 2 is from the TDT settling chamber downstream toward the test section. The four AOS vanes, the slots in the floor and the model centerline support sting can be seen. References [5, 9] discuss the AOS vanes in detail. Each vane utilizes a symmetrical airfoil section and has a span of 3.5 ft, a taper ratio of 0.5, and an aspect ratio of 1.2. The oscillation amplitude is adjustable from $0°$ to $\pm 12°$ while the frequency can be varied from zero to 20 Hz [6]. The oscillation amplitude and/or test section dynamic pressure are limited due to consideration of the design loads of the AOS vanes. At an oscillation frequency of 20 Hz, the combined limit varies from a dynamic pressure of about 60 psf at $12°$ vane amplitude to about 350 psf for $3°$ vane amplitude [4]. The two vane sets can be operated either in-phase or up to $180°$ out-of-phase. The oscillatory flow in the center of the test section is produced by the trailing vortices from each vane tip as the vortices alternate in rotation direction. The wavelength and general characteristics of the disturbance field are dependent upon frequency and free-stream velocity. The experimental data presented in this report are found in references [4–6].

III. Experimental Data Sets

The primary purpose of this paper will be to validate the CFD model of the combined tunnel, plenum and AOS with experimental TDT data of the AOS in operation. A secondary purpose is to assess the usefulness of the various data sets. Several papers have been published in the 1960s that present test section flow angle measurements due to AOS sinusoidal oscillation. Both hot-wire anemometers and fast-response probes were used to measure the oscillating flow components in order to observe the variation in flow angle. The published experimental data consist mostly of measurements of the amplitude of the vertical flow angles at selected points. Figure 3 shows the definition of vertical flow angle. The coordinate system is also shown, the origin of which is at the start of the contraction section upstream of the test section. Station 72 ($x = 72$) is shown as well. Most measurements were taken along a lateral (horizontal) line traversing the test section ($z = 0$) or at the center of the test section ($x = 72$ ft, $y = z = 0$). See Figure 2 for the orientation of the y and z axes. The phases of the test section flow angles are relative to the vane angle. The available data sets are summarized in Table 2. Experimentally measured data from the references identified in Table 2 are reproduced in Figures 4 through 8. It should be noted that there are more experimental conditions represented here than it has been possible to perform computations.

There are some general features in the experimental data to be noted. The Mach number range in the various reports spans from a nearly incompressible low Mach number at low dynamic pressures to Mach 1.1 at a significantly higher dynamic pressure. At all Mach numbers, the oscillation amplitude of the vertical flow angle at the test section centerline decreases with increasing AOS frequency. This is seen in all data sets, shown in Figures 4-6. Reference [6] reports that the vertical flow angle amplitude at low frequencies decreases somewhat with increasing Mach numbers

equal to or greater than Mach 0.80. Figure 6a shows this drop-off of vertical flow angle amplitude at Mach 0.80, 1.0, 1.1 measured at the test section centerline for $\omega/V < 0.1$ rad/ft. Reference [5] points to data showing the vertical flow angle amplitude at the test section center to be roughly proportional to the vane amplitude, thus providing a means to estimate and control the amount of test section excitation. Figure 6b indicates the cyclical variation of phase with increasing frequency indicative of a convecting flow measured at a distance from the source. The equation in Figure 6b defines one cycle of phase shift.

Since the test section velocity perturbations are created by trailing tip vortices and vane downwash, a quite large variation in the velocity across the test section can be expected. The experimental data references suggest that for a wind tunnel model to be exposed to a relatively homogeneous vertical flow velocity amplitude in the test section, a centerline mount should be used with no larger than a 6 ft-span model. Outboard of ± 3 ft about the centerline large variations in vertical flow angle amplitude and phase are observed. A moderately uniform oscillatory flow amplitude can be found in the test section having a depth of 4 ft [4]. There is some evidence in the experimental data of modest cross sectional variations in vertical flow angle amplitude within this region [5]. This is seen in Figure 4 at Mach 0.6, Figure 5 at Mach 0.22 and Figure 7 at Mach 1.00. The cause of those variations is not known. The Mach 1.00 data set provides flowfield vertical angle amplitude (Figure 7) and phase (Figure 8) along a line ± 3 feet laterally from the test section center line. There is also a set of data along lateral lines at the test section centerline height as well as 2 feet above and below the centerline height. These data indicate some variation in the vertical flowfield angle also along the z-axis, but uniform vertical flow angle phase relative to the vanes above and below the centerline height.

There is evidence of a resonance reported in reference [6] to be above a frequency of about 14 Hz for some Mach numbers. If resonance starts at 14 Hz for all Mach numbers, then in heavy gas, omega/V âĽě 0.7 rad/ft at Mach = 0.22, omega/V âĽě 0.24 rad/ft at Mach = 0.60, and omega/V âĽě 0.20 rad/ft at Mach = 0.80 [5, 6]. In air, these would be roughly half their heavy gas values. These reduced frequencies are consistent with the cut off frequencies stated in the studies due to resonance. The cause of this resonance has not been investigated, nor is the frequency and Mach number dependence clearly defined in the experimental data. There is also a potential conflict between the two low Mach number data sets. Reference [6] reports that at Mach 0.22 in R-12 for $\omega/V \leq 0.168$ rad/ft there is almost no phase shift whatsoever in the test section velocities relative to the AOS vanes. Reference [4] reports phase shifts in the range of $120 - 180°$ in that reduced frequency range at Mach 0.27 in air. The reason for this phase shift disparity may need to be investigated in future work.

IV.   AOS CFD Model

As discussed previously, the plan view of the TDT is shown in Figure 1. The red line around the test section leg of the tunnel shows the outline of the computational domain used in the CFD analysis. The approach used to obtain the surface geometry of the TDT was 'as-built' as opposed to 'per drawing'. To obtain 'as-built' geometry, a laser scan of the facility interior was conducted. The four vanes were laser scanned while they were uninstalled from the tunnel. Figure 2 shows the resulting computational surface looking down stream from the settling chamber at the installed AOS vanes.

The domain begins with the settling chamber and continues into the test section, where it is connected with the plenum via slots in all four walls. The domain ends with the diffuser section. The shape of the computational domain at the settling chamber is not desirable for the numerical analysis because of the corners where the east and west walls of the settling chamber meet the turning vanes. However, to include the geometric complexity of the turning vanes in the computational model, together with the rest of the tunnel geometry, is too computationally expansive. Therefore, a planar inflow boundary condition is set at the turning vanes location.

The unstructured tetrahedral volume meshes were generated using VGRID. The tetrahedral elements within the boundary layer were converted into prism elements with the first cell height away from the wall set to ensure the average y+ < 1. Information about the coarse and medium meshes are found in Table 1. At this time, only coarse and

medium mesh results have been completed. Figure 9 shows the mesh distribution over the tunnel and plenum walls as well as the location of the AOS vanes. Figure 10 shows the mesh distribution across the test section at station 72. The main difference between the coarse and medium meshes is in the refinement of the interior of the tunnel. The current mesh refinement strategy is to refine a single cylindrical region that encompasses the full interior of the tunnel. No attempt has been made to focus grid resolution on regions of high flow gradients.

Figure 11 shows the AOS vanes in a zero and $-12°$ deflection position. The vane deflection is accomplished by a modal shearing surface having z-deflection only. This should be sufficiently valid for the deflection angles necessary in this study. To maintain surface mesh continuity, the vane deflection decays on the surface linearly away from the vanes to a distance of 3-4 feet in each direction. The vane z-deflection is held constant in the region between the two vanes. It can be seen that the wind tunnel surface motion causes some distortion in the AOS mechanical housing, particularly in the trailing edge region of the vane. Without the use of chimera grids to facilitate the vane rotation, some distortion will be unavoidable to maintain surface integrity. The wall distortion should not have a significant influence on the test section turbulence especially near the centerline.

V.   CFD Method

The FUN3D software, to be used in these analyses, was developed at the NASA Langley Research Center. It is a finite-volume, unstructured-grid, node-based, mixed-element Reynolds-averaged Navier Stokes (RANS) and hybrid-RANS solver [10]. Various turbulence models are available, but in this study, the turbulence closure will be obtained using the Spalart-Allmaras (SA) one-equation model and the Modified Delayed Detached Eddy (MDDES) model. Inviscid fluxes are computed using the Roe flux difference splitting scheme with no flux limiter. The total pressure and total temperature boundary condition are used at the inlet, which is at the corner of the settling chamber (See Figure 9). At the exit to the computational domain (the diffuser section), a back-pressure boundary condition is used. The value of this back pressure is iterated to achieve the desired Mach number in the test section. In a typical solution, the entire flow field is initialized to the total pressure and total temperature in the settling chamber and to the static pressure elsewhere.

VI.   CFD Results

The experimental sets shown in Figures 5 at Mach 0.22 and in Figure 6 at Mach 0.80 will be used to validate the computational model. The data at Mach 0.22 provides a comparison of vertical flow angles across the test section laterally while the data at Mach 0.80 illustrates the dependence of vertical flow velocity angles on vane frequency. A tunnel cross section with flow contours in Figure 12 will orient the reader to the computational region of interest for data comparisons. The test section analysis region at tunnel station 72 is located 49.5 ft downstream of the quarter chord of the AOS vanes. The orientation of the test section coordinate system is shown in Figure 12. Also shown are contours of the amplitude of vertical flow angle in degrees. The vertical plane cut through one of the vanes and running the tunnel length shows an instantaneous snapshot of the oscillatory wake downstream of the AOS vanes. The test section cross plane at station 72 shows the dramatic variation in the velocity across the test section. The wake of the vanes is confined to within several feet of each side wall. Downwash from the tip vortices can be seen $4 - 5$ feet from either side wall and 3 feet above the y-axis.

All the simulations were carried out so that there were at least 8 cycles of AOS vane oscillation. In a few cases, additional cycles were needed to reach a fully converged centerline vertical flow angle amplitude. As shown in Table 1, the time step size is set to give 512 time steps per cycle in the coarse mesh and 1024 time steps per cycle in the fine mesh. The vertical flow angle amplitude and phase at the vane frequency are computed by a fast Fourier transform (FFT) for each point over the test section from which selected points are extracted. Vertical flow angle phase with respect to the vane oscillation are obtained. The amplitude of streamwise vorticity is also obtained by an FFT. All the

4

experiments were performed with R-12 heavy gas while the present computations were obtained for R-134a heavy gas. The values of the gas constants of R-12 and R-134a are very similar.

The computed amplitude of the vertical flow angle measured across the test section at $z = 0$ at Mach 0.22 will be shown first and compared to experimental data from reference [6]. The dynamic pressure for this case is 53 psf. The AOS amplitude is 5.93 degrees. These results are shown in Figure 13. The experimental data shows an asymmetric lateral spatial variance in flow angle that has been discussed earlier in this work, whereas both the coarse and medium meshes show almost complete symmetry about the $y = 0$ plane. Both meshes show the dependence of amplitude on frequency; the medium mesh follows the experimental data much more closely than does the coarse mesh.

The AOS vane tip vortices are the primary mechanism to produce the vertical velocity at the center of the test section. The mesh resolution of the vortex trail and vane wakes is critical to accurately simulating the centerline flow characteristics. The contour plot of vertical flow angle amplitude over the center part of the test section shown in Figure 14 illustrates the influence of vane wake and vortex core mesh refinement on the overall test section velocity field. The coarse mesh results (Figure 14a) show completely diffused vortices and a fairly smooth variation of flow angle amplitude over the entire test section. This would account for the higher centerline flow angle for the coarse mesh. Conversely, the vortex cores are less diffuse, more compact, in the medium mesh solution (Figure 14b) resulting in lower downwash velocities, and therefore lower flow angle amplitudes, at the center of the test section and much more variability over the outer portion of the test section. These results suggest that the medium mesh provides significantly more accurate simulation of the test section flow angle field generated by the AOS. From this point onward, unless otherwise stated, results will be for the medium mesh. However, it is clear from Figure 13 that neither mesh fully resolves the flowfield.

The dependence of test section flow angle amplitude on vane frequency is shown in Figures 15-18 for the case at Mach 0.80 with vane amplitude of 9°. These results are from simulations of the condition presented in reference [4], data for which are shown in Figure 6. This figure presents test section centerline ($y = z = 0$) oscillatory vertical flow angle amplitude and phase. The experimental data shows a strong decrease in test section oscillatory vertical flow angle amplitude with increasing vane frequency. The Mach 0.80 data in Figure 6 also shows a slight reduction of the negative slope for $\omega/V > 0.2$ rad/ft. It is unclear what is causing that slope change. It is therefore of interest to investigate whether the computational results also show a similar behavior. The cyclical phase variation of the experimental data with frequency also follows the behavior expected of a convecting flow. This can be seen in Figure 6b.

The Mach 0.80 experimental data are reproduced in Figure 15 alongside computational results. As with the Mach 0.22 case, the coarse grid greatly overpredicts the amplitude of the centerline flow angle. The phase of the centerline flow angle seems to be little affected by crossflow mesh resolution. The phases of both the coarse and fine meshes correlate well with the experimental data. The medium mesh flow angle approaches the experimental data, although for $\omega/V > 0.22$ rad/ft the two data sets diverge somewhat. The flow angle amplitude of both the coarse and medium meshes plateau in the range $0.22 < \omega/V < 0.30$. It is not clear what causes the plateaus. It is possible this is due to the tunnel resonance discussed in the experimental results, indicated for Mach number 0.80 to be at a frequency of $\omega/V \geq 0.20$ rad/ft. In the experimental data at Mach 0.80, the plateau is nothing more that a slight change in slope above this frequency.

Figure 16 shows contours of amplitude and phase of the oscillatory vertical flow angle at $\omega/V = 0.15$ rad/ft. Figure 17 shows contours of amplitude and phase of the oscillatory vertical flow angle at $\omega/V = 0.33$ rad/ft. The left hand plots in Figures 16 and 17 show the amplitude of the vertical flow angle. The figures show the downwash behind the vanes and tip vortex induced flow due to the AOS vanes at the two frequencies. The $\omega/V = 0.15$ rad/ft case tip induced vortex velocity peaks are at $z = \pm 2.1$ ft while the $\omega/V = 0.33$ rad/ft velocity peaks are at $z = \pm 3$ ft. Increased frequency causes the tip vortex and its induced flow to move further away from the $z = 0$ centerline and decrease in intensity. The downwash from the AOS vanes also moves farther from the $z = 0$ centerline and appears to intensify with increasing frequency.

5

The right hand plots in Figures 16 and 17 indicate the phase of the oscillatory vertical flow angle with respect to the AOS vane. There is an inflection point at the vane tips ($y \approx \pm 4.6$ ft) in each case. As expected for lift inducing vanes, the phase of the vertical flow angle changes roughly 180° at the y locations of the AOS vane tips. The phase change in the high frequency case is strongly discontinuous at that point, specifically at $z = \pm 3$ ft when the tip vortex is strongest. The phase of the downwash flow behind each vane ($y > 4.6$ ft and $y < -4.6$ ft) generally remains intact over the entire vertical extent of the test section. For the higher frequency case, the downwash behind each vane is more intense and is convected higher/lower than for the low frequency case. The variation of the features of these flow fields with frequency likely contributes to the decrease of the centerline vertical flow angle with increasing frequency.

Figure 18 offers more insight into the reason for this frequency dependence. These contour plots show the oscillatory amplitude of the vorticity over a cross-sectional plane at station 72. Figure 18a shows the vorticity vield for $\omega/V = 0.15$ rad/ft. Figure 18b shows the vorticity vield for a higher frequency at $\omega/V = 0.33$ rad/ft. At $\omega/V = 0.15$ rad/ft the cores of the tip vortices are stronger and closer to $z = 0$ as well as laterally closer to the centerline than at $\omega/V = 0.33$ rad/ft. Obviously the stronger vertical convection of the vane downwash in the higher frequency case also drives the tip vortex away from the $z = 0$ centerline. This would account for the reduction of the vertical flow angle at the tunnel centerline as the frequency increases. The small hash marks in each figure shows the location of the sidewall slots. It is interesting to note that there is much stronger flow around the sidewall slots at higher frequency as indicated by vorticity hot spots.

VII. Conclusions

This paper assesses the level of mesh refinement necessary to accurately simulate the operation of the Airstream Oscillation System of the Transonic Dynamics Tunnel. While the mesh refinement strategy has been hand-crafted, with cylindrical refined mesh region placed in the center of the tunnel, it has nonetheless shown that it should be possible with a carefully refined mesh, to accurately model the test section unsteady flow field. The medium mesh in the present work has come remarkably close to matching the experimental data.

The present results confirm the drop in centerline oscillatory vertical flow angle amplitude with increasing frequency. The computed phase shift as vane frequency changes matches the experimental data very well. The decrease in centerline vertical flow angle amplitude with increasing frequency has been shown to be related to the weakening of vane tip trailing vortices as they move away from the test section centerline. The computed results have confirmed that there is a plateau or slope change for $\omega/V > 0.2$ at Mach 0.80 seen in the experimental data. Currently the reason for that plateau is not known.

Once either a generally refined mesh or one with flow field targeted refinement is available, there are a number of additional studies that would be useful. The experimental data are limited to a few Mach numbers. It is of interest to investigate whether the flow angle versus frequency behavior at Mach 0.80 can be reproduced at other Mach numbers. Additional Mach numbers, especially in the transonic range, would merit computational investigation. A quantification of Mach number, frequency and vane amplitude effects would be useful. It would also be useful to explore the supposed resonance observed in the experimental and computational data as well as the potential influence of AOS vane dynamic stall on test section flow angles. There are also some apparent inconsistencies in the experimental phase data that merit exploration.

Beyond these additional studies, further computational efforts will be directed at modeling a test article installed with the AOS active. The upcoming Integrated Adaptive Wing Technology Maturation test would be an ideal opportunity to simulate simultaneously the AOS-generated gust field in the TDT test section and the gust response of an aeroelastic model due to that gust field.

References

[1] Chwalowski, P., Quon, E., and Brynildsen, S. E., "Computational Analysis of the Transonic Dynamics Tunnel," *54th AIAA Aerospace Sciences Meeting and Exhibit*, No. 2016-1775, January 4-8 2016.

[2] Chwalowski, P., Silva, W., Wieseman, C., and Heeg, J., "CFD Model Of The Transonic Dynamics Tunnel With Applications," *NATO AVT-284*, 2018.

[3] Chwalowski, P. and Ivanco, T., "Modeling of an Atmospheric-Boundary-Layer Profile in Support of Experiments in the NASA Langley Transonic Dynamics Tunnel," *International Forum on Aeroelasticity and Structural Dynamics*, No. 2019-027, June 10-13 2019.

[4] Gilman, J. and Bennet, R. M., "A Wind-Tunnel Technique for Measuring Frequency-Response Functions for Gust Load Analyses," *Journal of Aircraft*, Vol. 3, No. 6, November-December 1966, pp. 535–540.

[5] Abbott, F. T., "Brief Description of the Characteristics of the Langley Transonic DDynamic Tunnel Airstream Oscillator," Tech. Rep. NASA-TM-82340, NASA, September 1968.

[6] Staff, "Langley Working Paper: The Langley Transonic Dynamic Tunnel," Tech. rep., 1969.

[7] Waite, J., Bartels, R. E., and Stanford, B., "Aeroelastic Model Development for the Integrated Adaptive Wing Technology Maturation Project Wind-Tunnel Test," *AIAA Aviation Forum*, No. 2020-2717, June 2020.

[8] Waite, J. M., Grauer, J., Bartels, R. E., and Stanford, B., "Aeroservoelastic Control Law Development for the Integrated Adaptive Wing Technology Maturation Wind-Tunnel Test," *AIAA SciTech Conference*, January 2021, to be published.

[9] Mirick, P. H., Hamouda, M.-N. H., and Yeager, W. T., "Wind-Tunnel Survey of an Oscillating Flow Field for Application to Model Helicopter Rotor Testing," Tech. Rep. NASA TM-4224, NASA, December 1990.

[10] "FUN3D Manual," 2020.

Table 1 Mesh Sizes and Simulation Time Steps.

Mesh	Nodes $(\times 10^{-6})$	Tets $(\times 10^{-6})$	T.S/cycle
coarse	44	259	512
medium	110	653	1024

Table 2 Available AOS data sets.

Case number	Mach Number	Reduced Frequency (rad/ft)	Amplitude (deg.)	Reference
1	0.22	0.056, 0.112, 0.168, 0.280, 0.392	5.93	[6]
2	0.6	0.10, 0.20	6	[5]
3	0.27, 0.80, 1, 1.1	0.083, 0.164, 0.247, 0.328	9	[4]
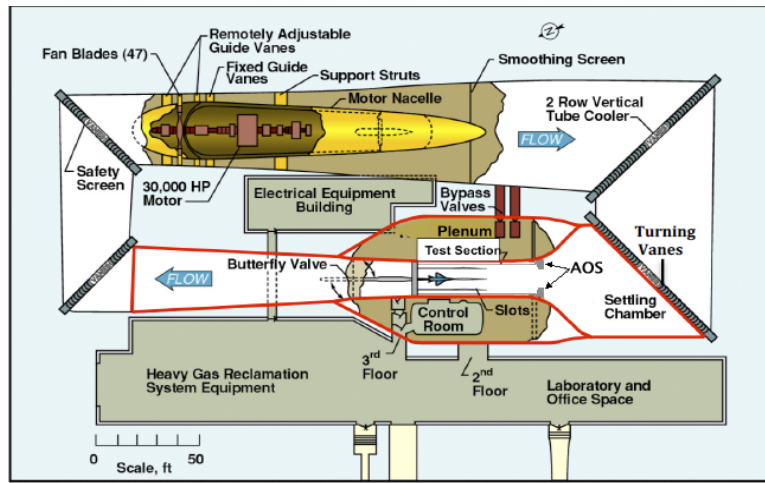
Fig. 1 Schematic of the Transonic Dynamics Tunnel with red outline indicating the computational domain.
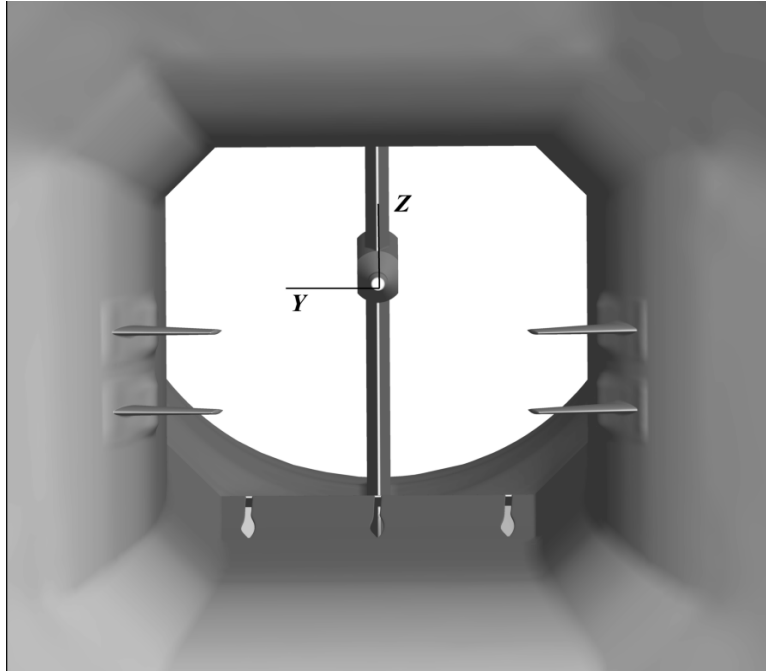
Fig. 2 Computational model of airstream oscillator looking downstream with test section floor, and sting mount in background.

$$\theta = \theta_0 \sin(\omega t + \phi)$$
θ_0 — Vertical flow angle amplitude
ϕ — Vertical flow angle phase

Station 72
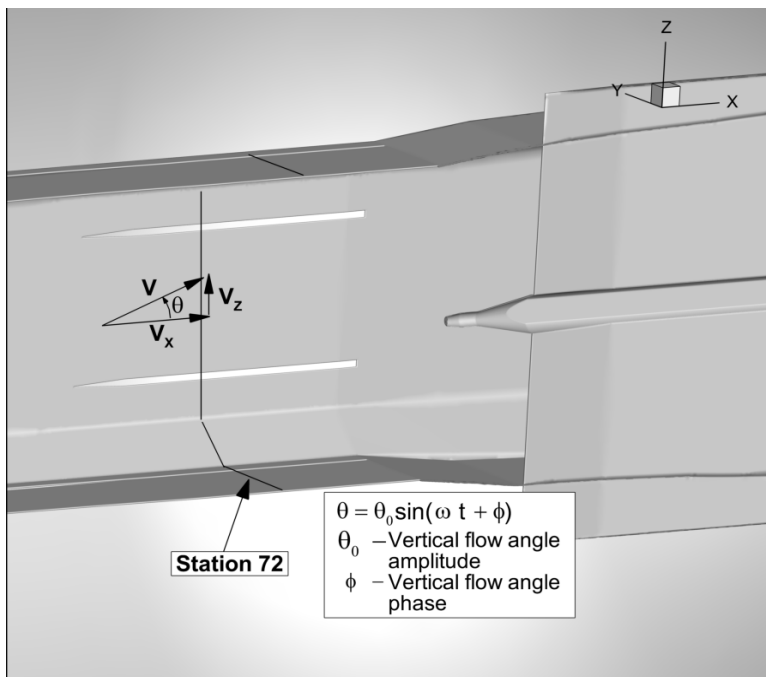
Fig. 3 Definition of vertical flow angle.
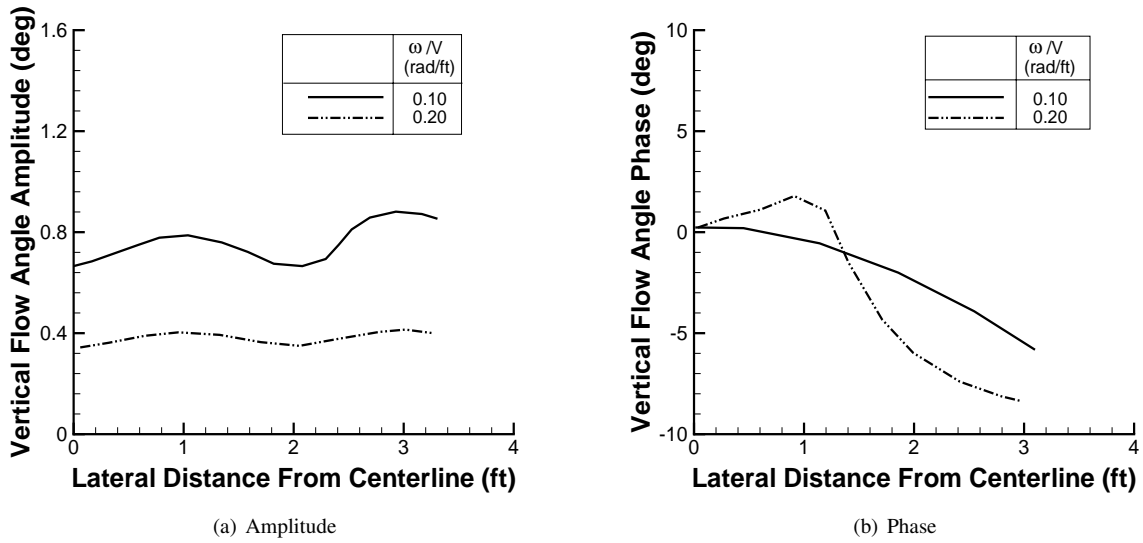
(a) Amplitude

(b) Phase

Fig. 4 Variation of the amplitude of vertical component of oscillatory flow angle and phase at tunnel test section centerline height in heavy gas R-12, Mach 0.6**, vane amplitude** 6°**. Experimental data from Ref. [5].**
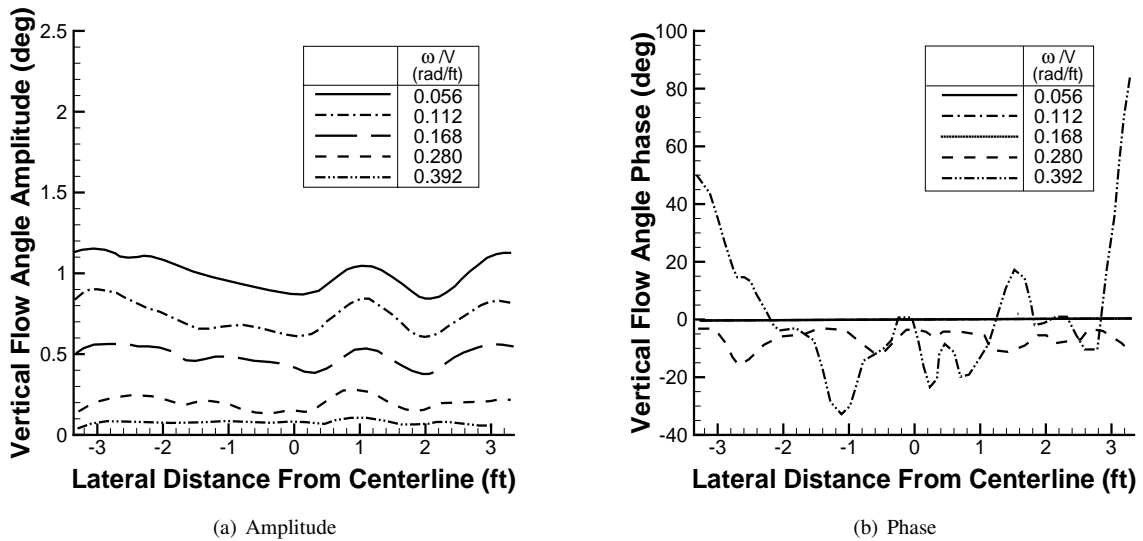
(a) Amplitude

(b) Phase

Fig. 5 Variation of the amplitude and phase of vertical component of oscillatory flow angle at tunnel test section centerline height in heavy gas R-12, Mach 0.22**, vane amplitude** 5.93°**. Experimental data from Ref. [6].**
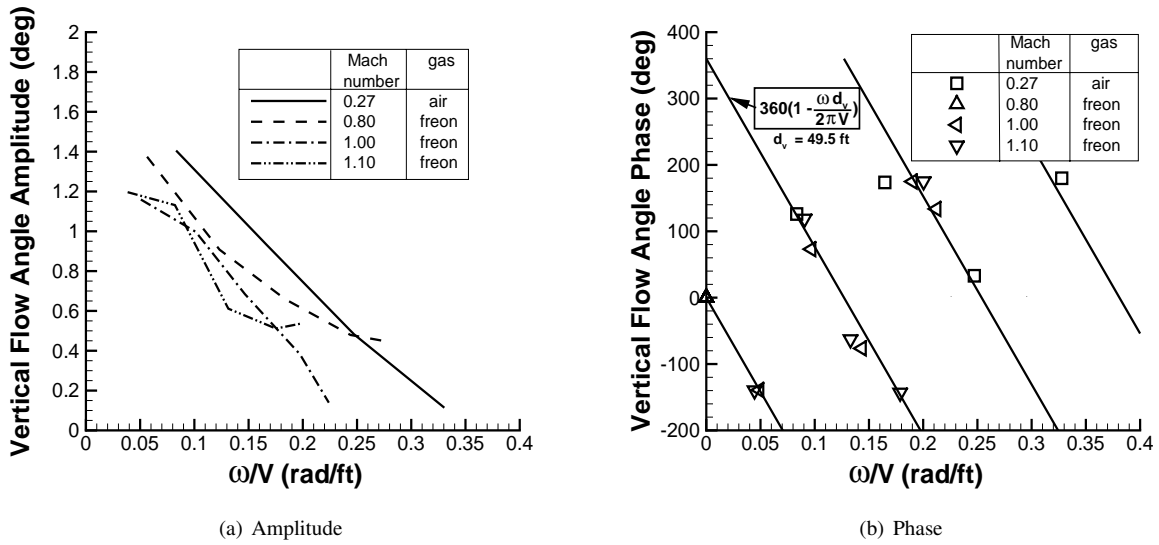
(a) Amplitude (b) Phase

Fig. 6 Variation of amplitude and phase of vertical component of oscillatory flow angle with AOS frequency at tunnel test section centerline height, vane amplitude $9°$**. Experimental data from Ref.** **[4].**
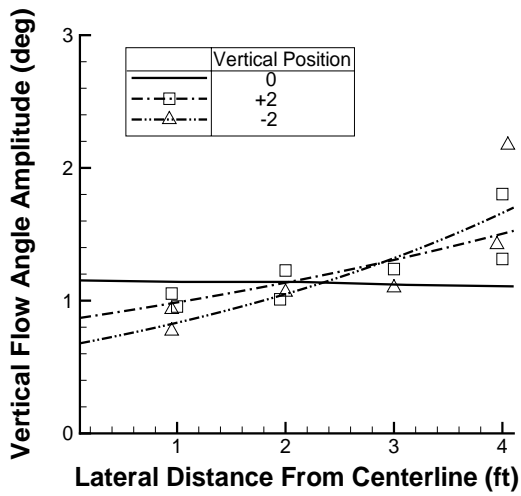
(a) $\omega/V = 0.049$ rad/ft
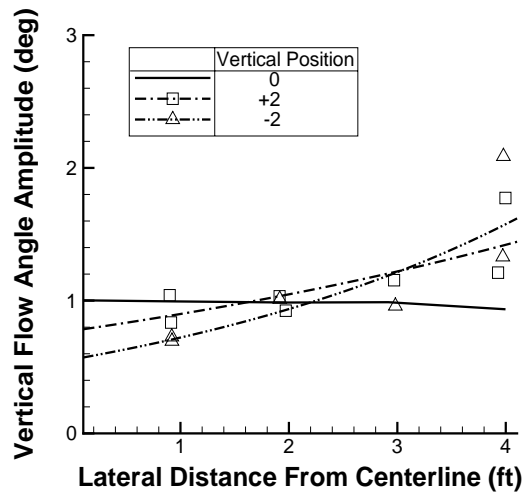
(b) $\omega/V = 0.098$ rad/ft
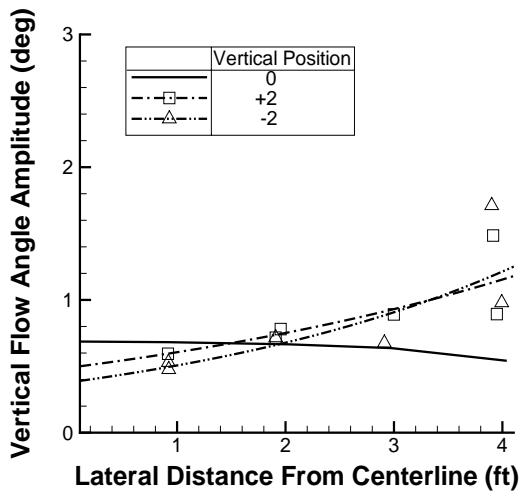
(c) $\omega/V = 0.146$ rad/ft
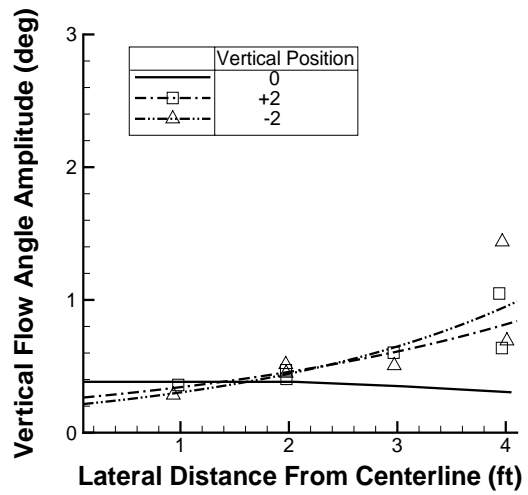
(d) $\omega/V = 0.196$ rad/ft

Fig. 7 Variation of the amplitude of vertical component of oscillatory flow angle with lateral position, Mach 1.00 **in heavy gas R-12, vane amplitude** 9°. **Experimental data from Ref. [4].**
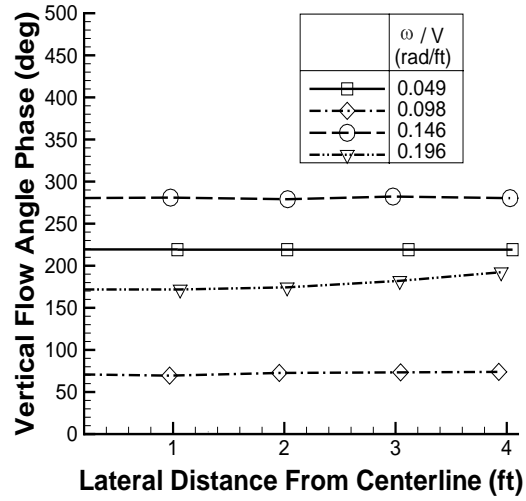
Fig. 8 Variation of oscillatory flow angle phase with lateral position, Mach 1.00 **in heavy gas R-12, vane amplitude** 9°**. Data from multiple heights combined since there is negligible variation with height. Experimental data from Ref.** [4]**.**
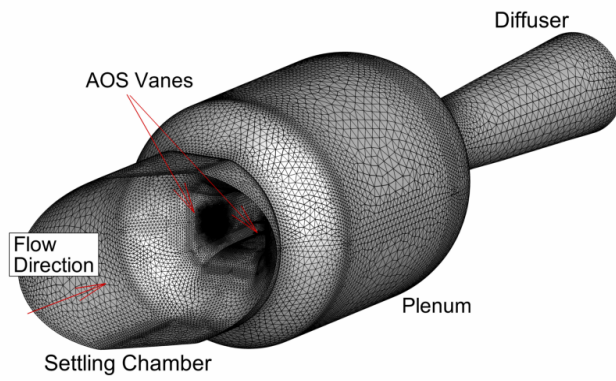
(a) Surface Mesh, coarse
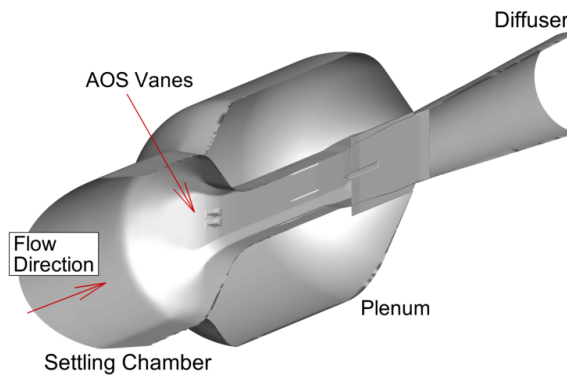
(b) Cross Section

Fig. 9 Computational model of TDT.

13

(a) coarse mesh

(b) medium mesh
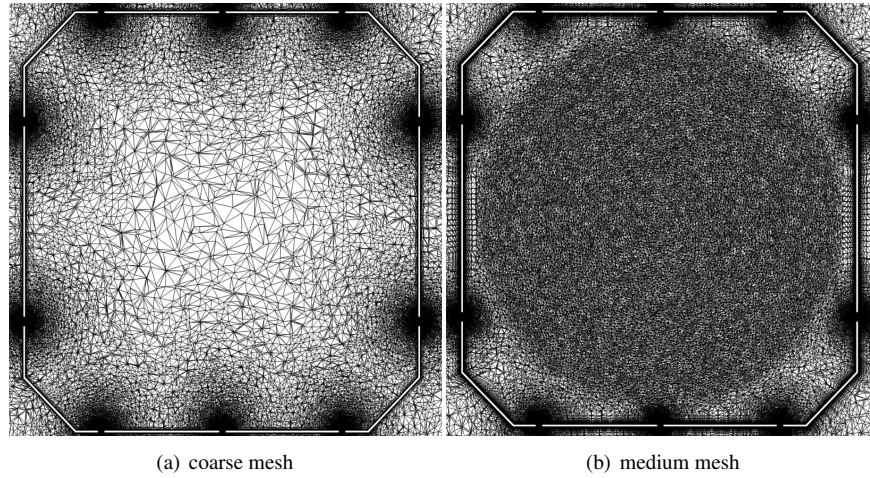
Fig. 10 Mesh distributions at Station 72.

(a) Zero deflection
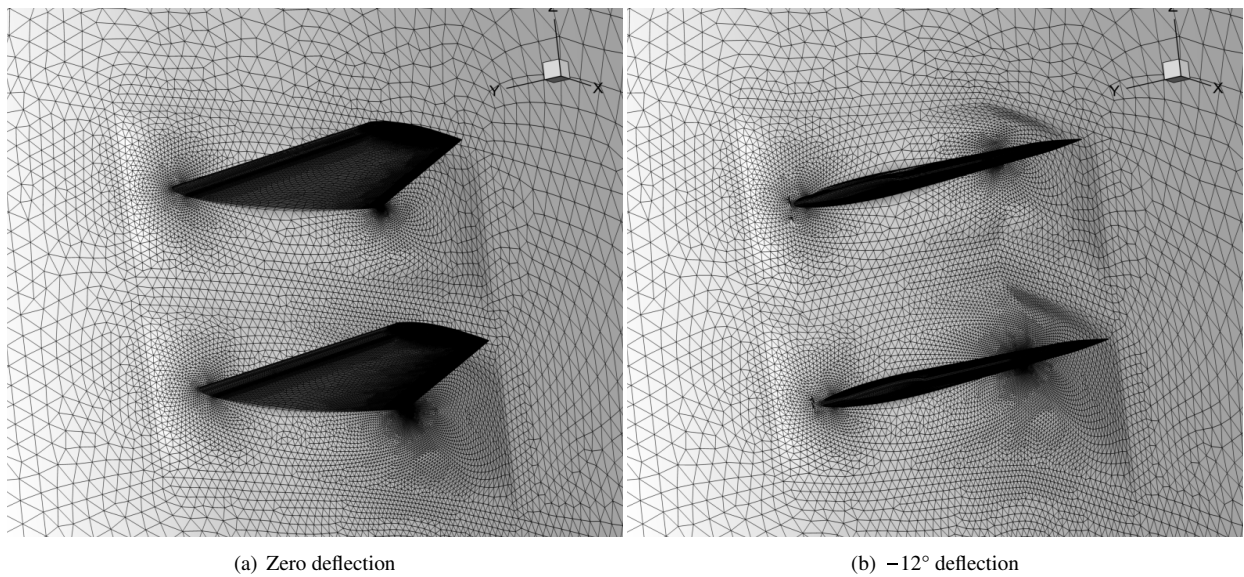
(b) −12° deflection

Fig. 11 AOS vane grid, undeflected and deflected, coarse mesh.
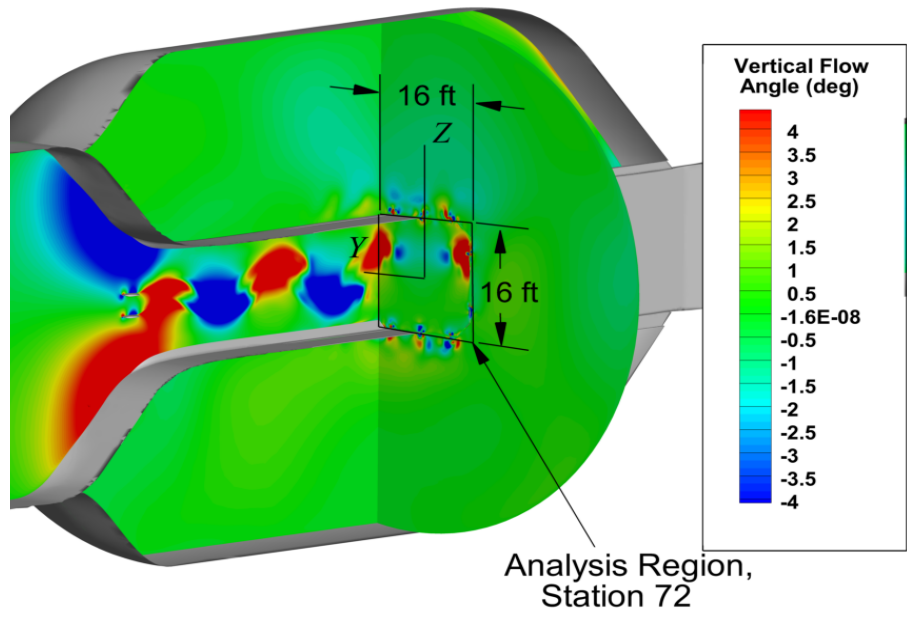
Fig. 12 Cross-section of Transonic Dynamics Tunnel with vertical flow angle contours.
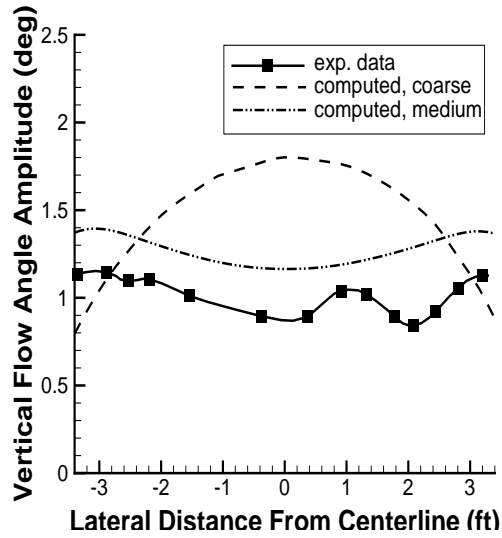
(a) $\omega/V = 0.056$ rad/ft.
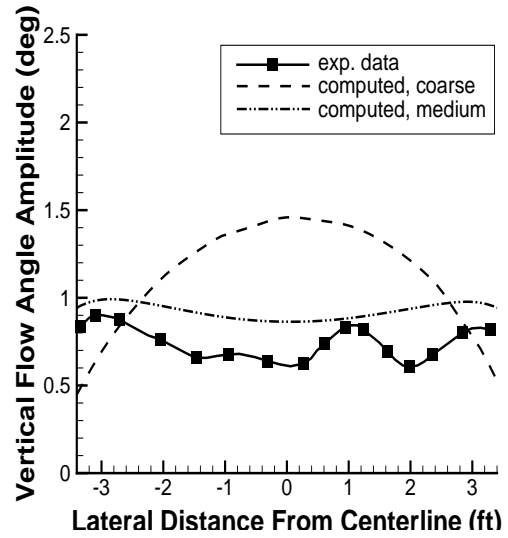
(b) $\omega/V = 0.112$ rad/ft
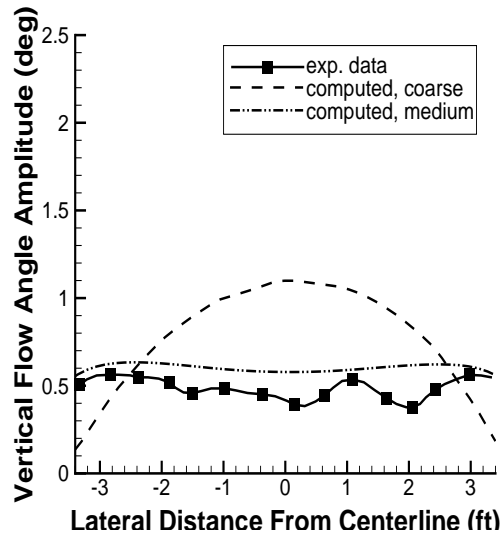
(c) $\omega/V = 0.168$ rad/ft

Fig. 13 Variation of the amplitude vertical component of oscillatory flow angle at tunnel test section centerline height, Mach 0.22 in heavy gas R-12, vane amplitude $5.93°$**, tunnel station 72. Experimental data from Ref. [6].**
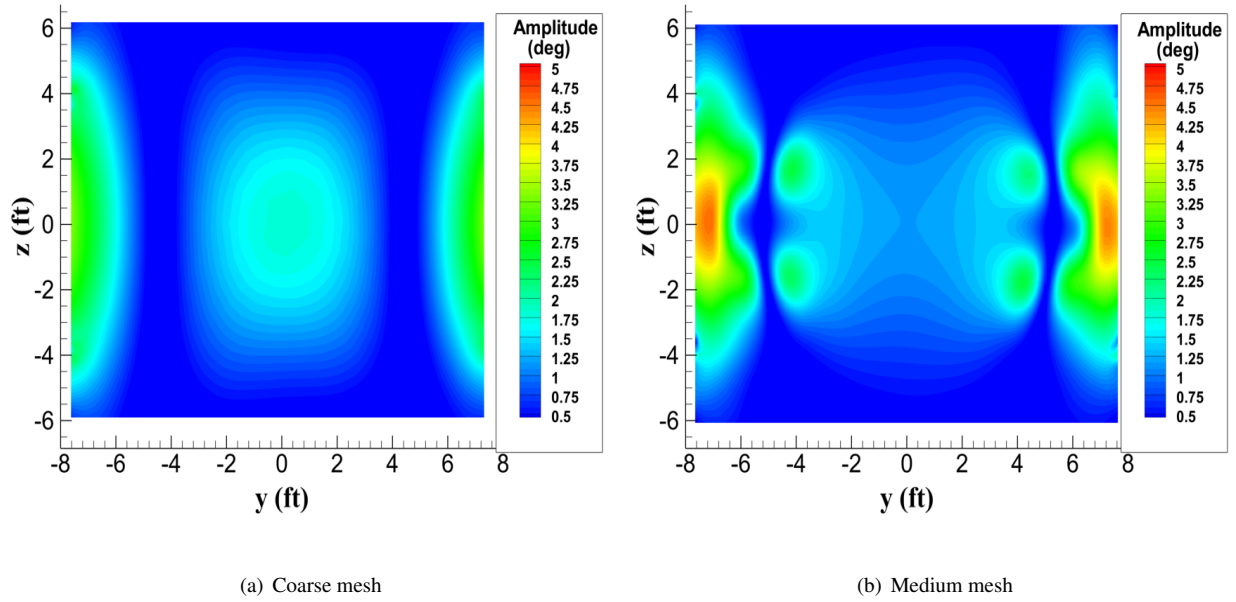
(a) Coarse mesh

(b) Medium mesh

Fig. 14 Contours of computed amplitude of vertical component of oscillatory flow angle , Mach 0.22 **in heavy gas R-12,** $\omega/V = 0.056$ **rad/ft, vane amplitude** $5.93°$**, tunnel station 72.**
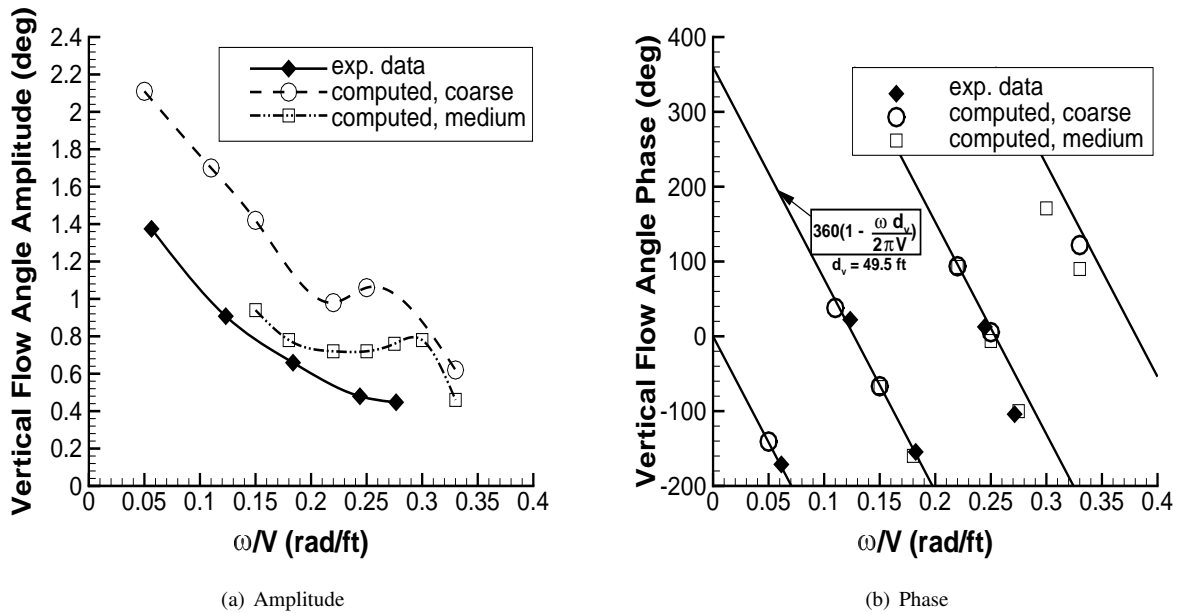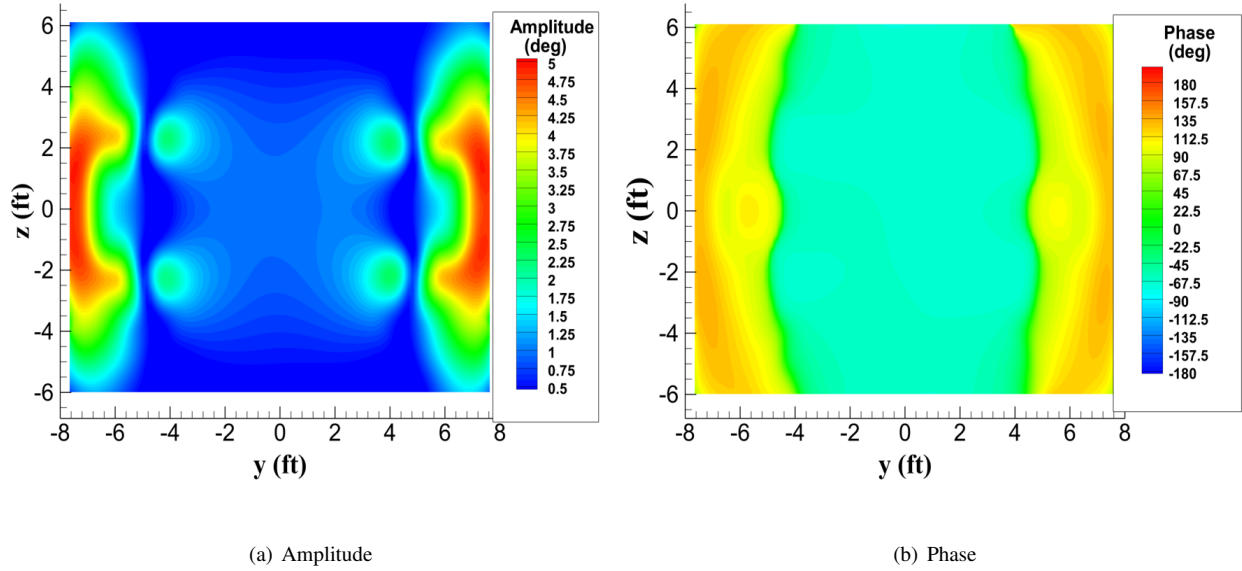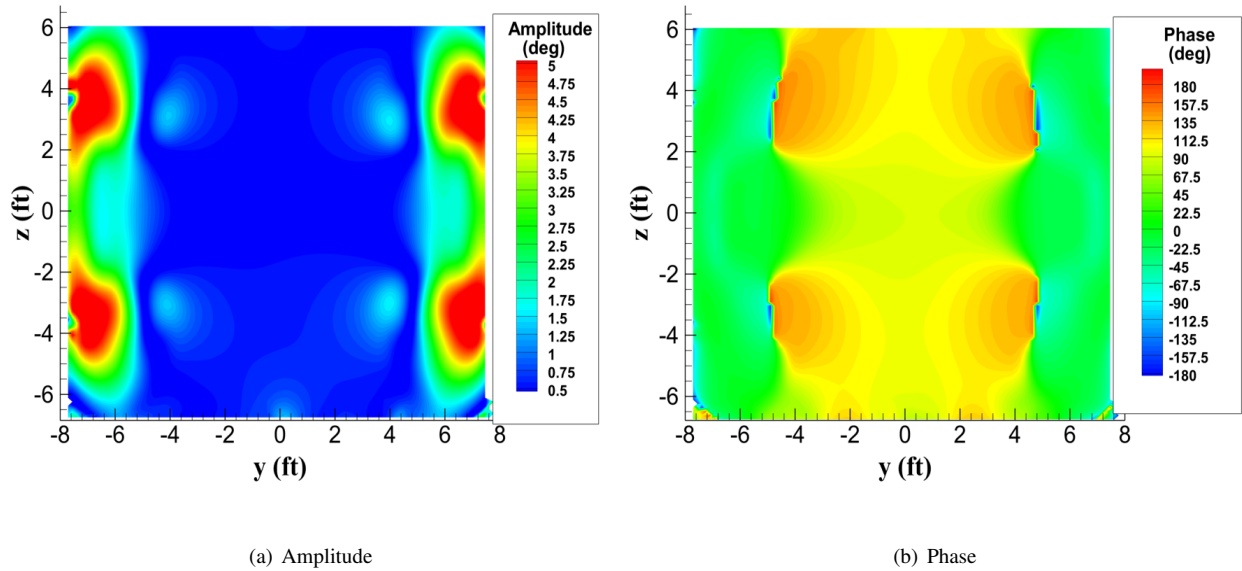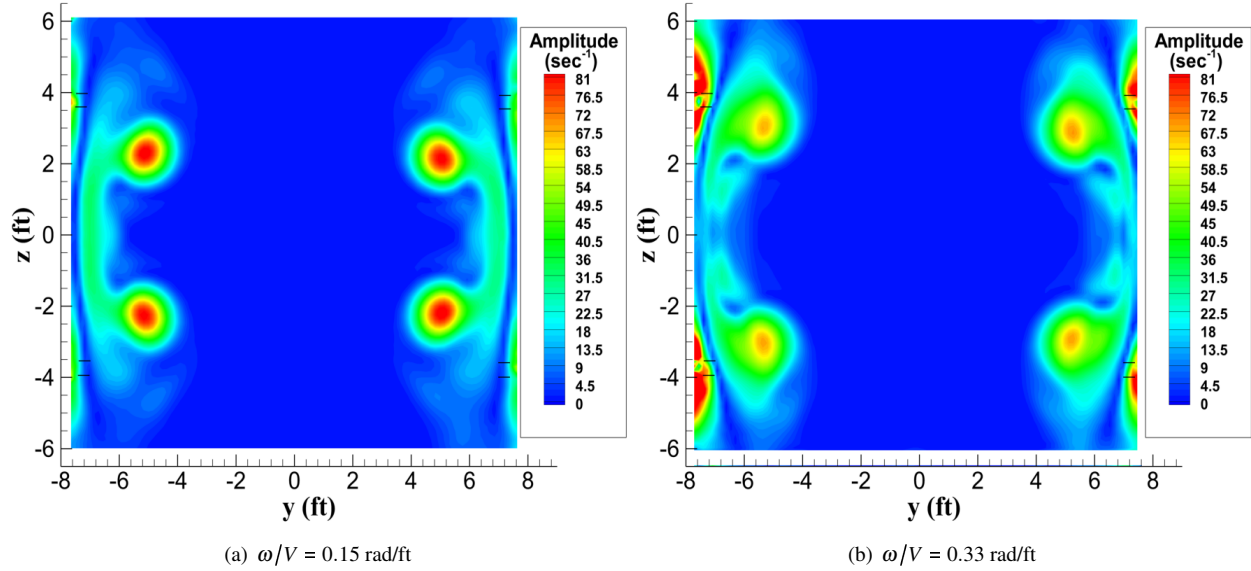

(a) Amplitude

(b) Phase

Fig. 15 Computed centerline oscillatory amplitude and phase, variation with frequency, Mach 0.80 **in heavy gas R-12, vane amplitude** $9°$**, tunnel station 72. Experimental data from Ref. [4].**

(a) Amplitude

(b) Phase

Fig. 16 Contours of computed oscillatory vertical flow angle, medium mesh, Mach 0.80 **in heavy gas R-12,** $\omega/V = 0.15$ **rad/ft, vane amplitude** $9°$**, tunnel station 72.**

(a) Amplitude

(b) Phase

Fig. 17 Contours of computed oscillatory vertical flow angle, medium mesh, Mach 0.80 **in heavy gas R-12,** $\omega/V = 0.33$ **rad/ft, vane amplitude** $9°$**, tunnel station 72.**

(a) ω/V = 0.15 rad/ft

(b) ω/V = 0.33 rad/ft

Fig. 18 Contours of computed amplitude of oscillatory vorticity, medium mesh, Mach 0.80 **in heavy gas R-12, vane amplitude** $9°$**, tunnel station 72.**